mater.scichina.com link.springer.com

Published online 15 December 2020 | https://doi.org/10.1007/s40843-020-1508-7
Sci China Mater 2021, 64(4): 808–819

Highly efficient organic solar cells enabled by a porous ZnO/PEIE electron transport layer with enhanced light trapping

Shenya Qu[1,2], Jiangsheng Yu[1*], Jinru Cao[2], Xin Liu[1], Hongtao Wang[1,2], Shun Guang[1,2] and Weihua Tang[2*]

ABSTRACT **In this study, a porous inorganic/organic (ZnO/PEIE, where PEIE is polyethylenimine ethoxylated) (P-ZnO) hybrid material has been developed and adopted in the inverted organic solar cells (OSCs). The P-ZnO serving as the electron transport layer (ETL) not only presents an ameliorative work function, but also forms the cratered surface with increased ohmic contact area, revealing suppressed charge recombination and enhanced charge extraction in devices. Particularly, P-ZnO-based OSCs show improved light trapping in the active layer compared with ZnO-based ones. The universality of P-ZnO serving as ETL for efficient OSCs is verified on three photovoltaic systems of PBDB-T/DTPPSe-2F, PM6/Y6, and PTB7-Th/$PC_{71}BM$. The enhancements of 8% in power conversion efficiency (PCE) can be achieved in the state-of-the-art OSCs based on PBDB-T/DTPPSe-2F, PM6/Y6, and PTB7-Th/$PC_{71}BM$, delivering PCEs of 14.78%, 16.57%, and 9.85%, respectively. Furthermore, a promising PCE of 14.13% under air-processed condition can be achieved for P-ZnO/PBDB-T/DTPPSe-2F-based OSC, which is among the highest efficiencies reported for air-processed OSCs in the literature. And the P-ZnO/PBDB-T/DTPPSe-2F-based device also presents superior long-term storage stability whether in nitrogen or ambient air-condition without encapsulation, which can maintain over 85% of its initial efficiency. Our results demonstrate the great potential of the porous hybrid P-ZnO as ETL for constructing high-performance and air-stable OSCs.**

Keywords: light trapping, electron transport layer, porous structure, stability, organic solar cells

INTRODUCTION

Organic solar cells (OSCs), as one of emerging photovoltaic technologies, have attracted enormous attention in view of their unique merits, such as semi-transparency, solution processability and mechanical flexibility [1–5]. A high power conversion efficiency (PCE) over 18% has been realized in single-junction OSCs due to the rapid progress associated with semiconducting materials and device innovations [6–9]. In view of photoactive material aspects, polymers or small molecules have been intensively investigated and developed along with the combination of binary or multicomponent donor/acceptor materials [10–19], and optimal nanoscale morphology of bulk-heterojunction (BHJ) active layers [20–24]. In the sandwiched device architectures, engineering and optimization of the interfaces between photoactive layer and metal electrodes are also crucial and challenging, which can promote the photogenerated charge carrier collection.

In the inverted devices, interfacial engineering of electron transport layers (ETLs) is widely exploited to implement high-performance OSCs [25–27]. Besides the principle of energy alignment between the photoactive layer and metal electrode, the high transparency and mobility of ETLs are also accounted [28–30]. Up to now, metal oxides such as zinc oxide (ZnO) and titanium oxide (TiO_2) are frequently served as ETLs to form ohmic contact for facilitating charge transport and collection [31,32]. The primary selective sol-gel ZnO is utilized in numerous efficient OSCs due to its high electron mobility (~5 $cm^2 V^{-1} s^{-1}$) and superior optoelectronic properties [33]. However, the intrinsic defects and charge traps always accompany each other at the surface and bulk of ZnO film depending on the thermal annealing process, which could lead to severe charge recombination [34]. To

[1] MIIT Key Laboratory of Advanced Solid Laser, Nanjing University of Science and Technology, Nanjing 210094, China
[2] School of Chemical Engineering, Nanjing University of Science and Technology, Nanjing 210094, China
* Corresponding authors (emails: yjs@njust.edu.cn (Yu J); whtang@njust.edu.cn (Tang W))

address these issues, many groups have been engaged to develop organic ETL materials for OSCs [35]. Recently, Lin *et al.* [36] have explored glucose-based biopolymers as zinc oxide surface modifiers for the inverted OSCs, and the methyl-cellulose-modified ZnO ETL can enable improved performance in devices. Pan *et al.* [37] have reported an N-doped (*N*,*N*-dimethyl-ammonium *N*-oxide) propyl perylene diimide-graphene (PDINO-G) as ETL through dispersing graphene in the alcohol-soluble PDINO, revealing the enhanced photovoltaic performance in several derived OSCs. Zhang *et al.* [38] have developed a novel interfacial cathode material, named as poly[(9,9-bis(3'-(*N*,*N*-dimethylamino)propyl)-2,7-fluorene)-alt-5,5'-bis(2,2'-thiophene)-2,6-naphthalene-1,4,5,8-tetracaboxylic-*N*,*N*'-di(2-ethylhexyl)imide] (PNDIT-F3N). The derived homojunction tandem OSCs have exhibited remarkable stability with efficiency retaining 93% of their initial value after thermally aging at 80°C for 1000 h.

To refine the interfacial contact of inorganic ETL, surface modifiers such as polyethylenimine (PEI) [39], PEI ethoxylated (PEIE) [40], and poly[(9,9-bis(3'-(*N*,*N*-diethylamino)propyl)-fluorene)-alt-2,7-(9,9-dioctyl-fluorene)] (PFN) [41] have also been exploited. Benefiting from the reduced work function and better compatibility of the optimized ETL, the relative OSCs reveal suppressed charge recombination with boosted overall photovoltaic performance. However, there is a fatal drawback, that is, these polar materials have inherently low electrical conductivity and thus are extremely sensitive to thickness [42,43]. For the high-throughput solution-coating process of OSCs, there is a delicate balance to select organic or inorganic interface materials. Considering the above trade-offs, developing the promising interface material with suitable work function and superior conductivity is still highly desired for efficient and stable OSCs.

In this study, an organic/inorganic hybrid ETL with porous structure (P-ZnO) has been successfully adopted in the inverted OSCs, which is composed of PEIE and ZnO. Herein, the PEIE was well dispersed in the ZnO precursor solution, and the spin-coated P-ZnO films were processed with thermal annealing for forming ZnO crystal, solvent washing for porous structure, and heating for cleaning in sequence. The P-ZnO serving as ETL not only presented an ameliorative energy alignment between the photoactive layer and cathode (indium tin oxide (ITO)), but also formed a unique surface with increased ohmic contact area. Three active layer composites, PBDB-T/DTPPSe-2F, PTB7-Th/$PC_{71}BM$ and PM6/Y6 were utilized to explore the efficacy of P-ZnO as ETL. Consequently, compared with ZnO-based counterparts, P-ZnO-based OSCs revealed enhanced photovoltaic performance with improved short-circuit current density (J_{SC}) and fill factor (FF), which accounted for the suppressed charge recombination and enhanced charge extraction. Besides, the P-ZnO-based devices also showed improved light trapping in the active layer due to the softened reflection at the interface. High PCEs of 14.78%, 9.85%, and 16.57% for devices based on PBDB-T/DTPPSe-2F, PTB7-Th/$PC_{71}BM$ and PM6/Y6 can be realized, respectively. Moreover, the devices based on P-ZnO/PBDB-T/DTPPSe-2F exhibited distinguished fabricating flexibility whether in the nitrogen (N_2) or ambient air condition, delivering comparative photovoltaic efficiencies and satisfactory long-term storage stabilities. A decent PCE of 14.13% for air-processed OSCs was achieved, which is among the highest efficiencies reported for air-processed OSCs in the literature.

EXPERIENTAL SECTION

Porous ETL preparation

The ZnO precursor solution was prepared by dissolving zinc acetate dihydrate ($Zn(CH_3COO)_2{\cdot}2H_2O$, Aldrich, 1 g) and ethanolamine (Aldrich, 0.14 mL) in 2-methoxyethanol (ME, Aldrich, 5 mL). The precursor solution was stirred overnight to yield a transparent solution. The 35 wt% PEI aqueous solution (PEIE, 80% ethoxylated, M_w ~70,000 g mol^{-1}, Aldrich) was diluted to 0.5% with ME and stirred overnight. Then ZnO precursor and dilute PEIE solutions were mixed with different volume ratios. The derived ETL films were spin-coated with the mixed solution at 5000 r min^{-1} for 30 s and annealed at 150°C for 30 min. Then the films were rinsed with ME at 3000 r min^{-1} for 30 s to form P-ZnO films, and heated for 10 min subsequently.

Device fabrication

All OSCs were fabricated with the inverted structure of ITO/ETL/active layer/MoO_3/Ag. ITO/glass substrates with a sheet resistance of 15 Ω sq^{-1} were ultrasonically cleaned with detergent, deionized water, acetone, and isopropanol for 15 min each, and subjected with oxygen plasma for 180 s for further cleaning. The pristine ZnO films were spin-coated with the ZnO precursor solution, which contained dissolved zinc acetate dihydrate (1 g) and ethanolamine (0.28 mL) in ME (10 mL). The ZnO/PEIE and P-ZnO films were spin-coated with the prepared mixed solution at 5000 r min^{-1} for 30 s, respectively. The BHJ blend films were processed as previously reported [44–46]. The MoO_3 (8 nm) and Ag (150 nm)

layers were successively deposited by thermal evaporation.

Characterization and device measurements

The current density-voltage (*J-V*) characteristics of all devices were measured under AM 1.5 G at 100 mW cm^{-2} irradiance (Oriel 300 W Solar Simulator) with a Keithley 2400 Unit. The light intensity was calibrated with a standard silicon diode (KG5 filter). The typical active area was 3.97 mm^2 as defined by a metal mask with an aperture. External quantum eciency (EQE) measurements were carried out from a Solar Cell Spectral Response Measurement System QE-R3011 (Enlitech Co., Ltd.) equipped with a standard Si diode. The film thicknesses were measured using Bruker Dektak XT stylus profiling system. The X-ray photoelectron spectroscopy (XPS) measurements were conducted using Thermo Scientific ESCALAB 250Xi spectrometer. The ultraviolent photoelectron spectroscopy (UPS) measurements were collected on a Thermo Fisher Scientific Ultra Spectrometer (ESCALAB 250Xi) He (I) (21.22 eV) radiation line from a discharge lamp. All measurements were performed at room temperature (296 K). The contact angle measurements of derived films were performed on SL200C optical contact angle meter (Solon Information Technology Co., Ltd.).

RESULTS AND DISCUSSION

Morphology characterization

To manufacture the P-ZnO films, a certain concentration of PEIE in ME was added to the ZnO precursor solution with a volume ratio of 1:2. After spin-coating with the prepared solution and thermal annealing, ME was utilized again to scour off PEIE component for forming porous structure as shown in Fig. 1a. The detailed process is summarized in Supplementary information. As shown in Fig. S1, a distinct porous structure in the designed film (P-ZnO) can be observed from optical microscope observation. To reveal the progress of porous structure of P-ZnO, the morphology features of pristine ZnO film, prepared ZnO/PEIE composite film without washing, and P-ZnO film were detected with the atomic force microscope (AFM) and scanning electron microscope (SEM) measurements as shown in Fig. 1b–g. The irregular morphology and the highest root-mean-squared surface

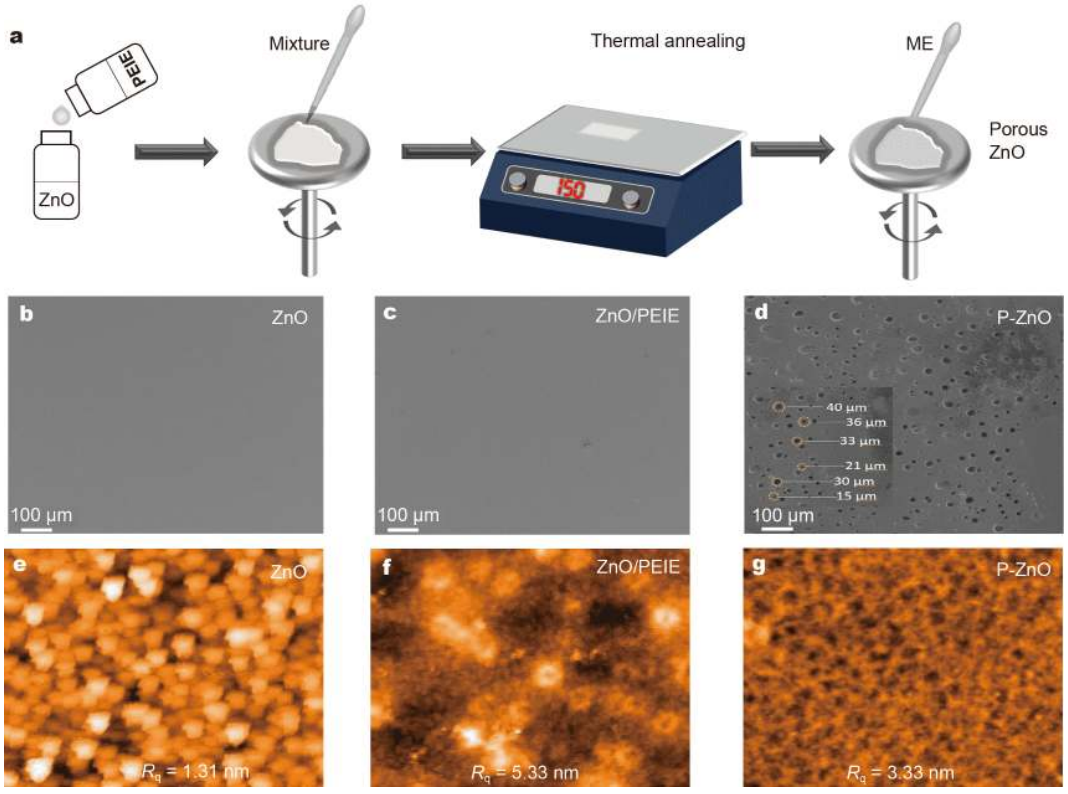

Figure 1 (a) The fabricating process of P-ZnO. SEM and AFM height images of (b, e) pristine ZnO film, (c, f) ZnO/PEIE composite film without solvent washing and (d, g) P-ZnO film.

roughness (R_q of 5.33 nm) of ZnO/PEIE film may result from the aggregation of PEIE on the surface. After solvent washing, the R_q of P-ZnO film shows a moderate value of 3.33 nm in the three films, which confirms the removal of PEIE component on the surface. Compared with the R_q value (1.31 nm) of pristine ZnO film, the proper increased surface roughness of P-ZnO film may enhance the ohmic contact, which is beneficial to the charge transport and electron extraction. As shown in the Fig. 1d, the diameter scale of porous size in the cratered P-ZnO film can be defined in 10–40 μm.

XPS analysis

In order to explore the composition of the derived films, XPS measurement was employed. Fig. 2 shows the narrow scans of N 1s, Zn 2p and O 1s core level spectra for ZnO, ZnO/PEIE and P-ZnO films. It is evident that N 1s peak can be observed in the P-ZnO film as shown in Fig. 2a, indicating the hybrid components of P-ZnO. The shifting binding energy of N 1s core level from pure PEIE (400.1 eV) to P-ZnO (401.6 eV) implies that chemical bonding could occur between PEIE and ZnO. The O 1s spectra were fitted with two Gaussian components as shown in Fig. 2b. The lower binding energy (530 eV) can be assigned to the divalent oxygen (O^{2-}) state, while the higher binding energy (532.5 eV) is related to the oxygen-deficient regions from the hydroxyl bonds on the surface, indicating the intrinsic defects in the films. As shown in Fig. 2c, the Zn 2p peaks of ZnO and P-ZnO are located at binding energies of 1044.4 and 1044.0 eV, respectively [47–49]. The lower binding energy of Zn 2P core level for P-ZnO also implies that PEIE can effectively passivate the defects of ZnO, which is favorable for the charge transport in P-ZnO-based devices.

Miscibility and work function analysis

The surface tensions and contact angles were measured to explore the miscibility of P-ZnO. As shown in Fig. 3a, the water contact angle is determined to be 36.0°, 35.4°, 27.5° and 22.2° for ZnO, P-ZnO, ZnO/PEIE and PEIE, respectively. The similar contact angles of ZnO/PEIE and PEIE films confirm the above speculation that the aggregation of PEIE would occur on the surface during the fabricating process of P-ZnO film. The nearly equal contact angles of pristine ZnO and P-ZnO films suggest ZnO crystal is dominant on the surface of hybrid P-ZnO

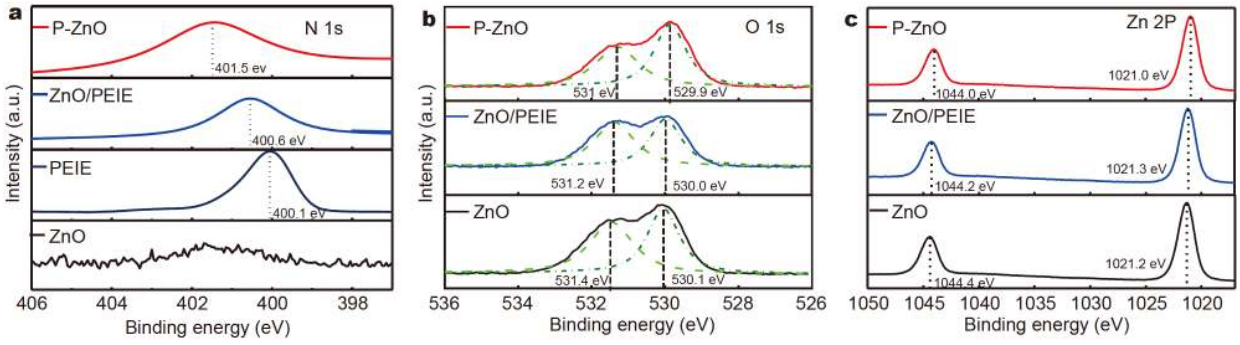

Figure 2 The high-resolution XPS spectra of (a) N 1s, (b) O 1s and (c) Zn 2P of pristine ZnO, PEIE, ZnO/PEIE and P-ZnO, respectively.

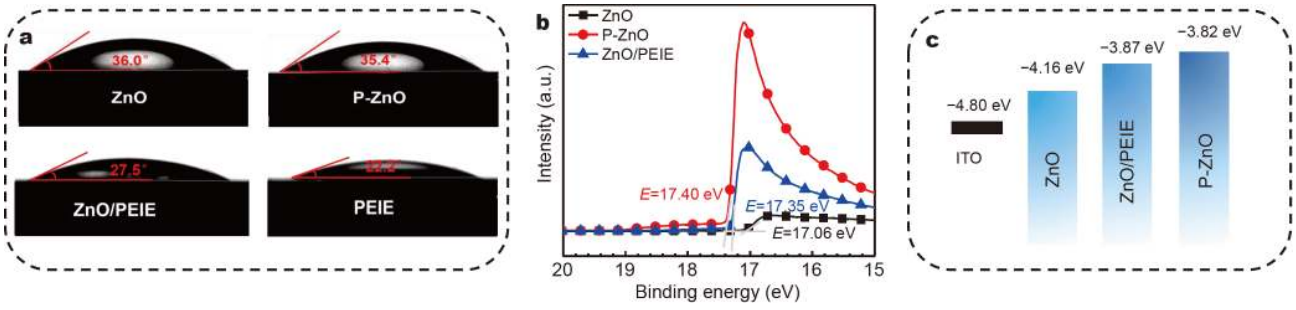

Figure 3 (a) Contact angle images on different ETLs. (b) UPS spectra and (c) the schematic energy diagrams of pristine ZnO, ZnO/PEIE and P-ZnO, respectively.

film. To explore the distribution of PEIE in the P-ZnO film, the XPS behaviors with P-ZnO layer of varying thicknesses (5 and 45 nm) were conducted as shown in Fig. S2. Clearly, N 1s peak at 45 nm presents an enhanced intensity, and the N atomic proportion at 45 nm is also higher than that at 5 nm. The results indicate that residual PEIE mainly exists at the bottom of P-ZnO which could prevent the direct contact between the active layer and ITO. The work function as the critical parameter of ETL was conducted with the UPS measurement. As shown in Fig. 3b, the binding energies of cut off region (E_{cutoff}) for ZnO, ZnO/PEIE and P-ZnO are 17.06, 17.35 and 17.40 eV, respectively. The work function value is calculated from the difference between E_{cutoff} and the energy of hv, where hv is the incident photon energy of He (I) source with a value of 21.22 eV. Consequently, the work functions of ZnO, ZnO/PEIE and P-ZnO are 4.16, 3.87 and 3.82 eV, respectively. The schematic energy diagrams are summarized in Fig. 3c. The results indicate that besides a porous structure film formed in the hybrid P-ZnO, a reduced work function of P-ZnO is also induced, which originates from the intrinsic molecular dipole of PEIE. It is beneficial to the charge transport and electron extraction in devices [50,51].

Photovoltaic performance

To explore the potential of P-ZnO serving as ETL, the photovoltaic performance of inverted OSCs was systematically investigated. The PBDB-T/DTPPSe-2F blend as shown in Fig. 4a was employed as the active layer, which was reported in our previous work [45]. As a comparison, the pristine ZnO, PEIE and ZnO/PEIE-based devices were also fabricated. The detailed *J-V* characteristics of OSCs are plotted in Fig. 4b and Fig. S3 and the related photovoltaic parameters are summarized in Table 1 and Tables S1–S3. The optimal condition for P-ZnO layer was found through tuning the concentration of prepared PEIE solution and volume ratio of ZnO/PEIE solution (0.5 wt%, 2:1). The pristine ZnO-based device presented a PCE of 13.65% with an open-circuit voltage (V_{OC}) of 0.84 V, a J_{SC} of 22.03 mA cm^{-2} and a FF of 73.77%. As shown in Fig. S3d, a decreased efficiency of ZnO/PEIE-based OSC

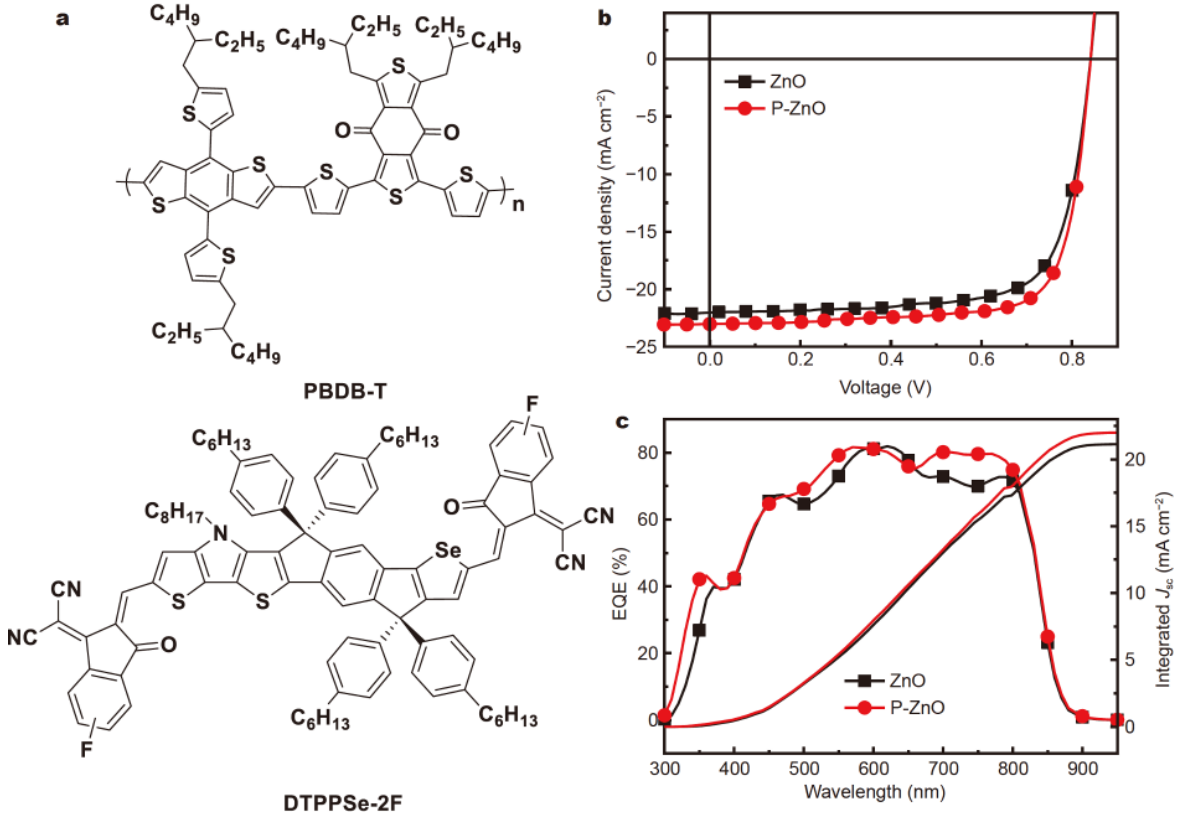

Figure 4 (a) The chemical structures of PBDB-T and DTPPSe-2F. (b) *J-V* curves and (c) EQE curves of PBDB-T/DTPPSe-2F-based OSCs with different ETLs.

Table 1 Photovoltaic parameters of OSCs with different ETLs

Active layer	ETL	V_{OC} (V)	J_{SC} (mA cm^{-2})	$J_{SC,cal}$[a] (mA cm^{-2})	FF (%)	PCE (%)
PBDB-T/DTPPSe-2F	ZnO	0.84(0.84±0.00)	22.03(21.92±0.12)	21.18	73.77(73.57±0.16)	13.65(13.50±0.15)
	P-ZnO	0.84(0.83±0.01)	22.96(22.87±0.06)	22.21	76.62(76.15±0.53)	14.78(14.56±0.23)
PM6/Y6	ZnO	0.85(0.85±0.00)	24.93(24.82±0.12)	24.07	72.57(71.93±0.61)	15.38(15.22±0.15)
	P-ZnO	0.85(0.85±0.00)	25.70(25.52±0.13)	24.80	75.84(75.37±0.42)	16.57(16.42±0.13)
PTB7-Th/$PC_{71}BM$	ZnO	0.80(0.80±0.00)	16.70(16.35±0.19)	15.54	68.32(67.27±0.18)	9.12(8.91±0.25)
	P-ZnO	0.80(0.80±0.00)	17.26(17.07±0.13)	16.22	71.31(70.98±0.42)	9.85(9.72±0.13)

a) The values are integrated J_{SC} from EQE spectra. Optimal and statistical results are listed outside.

was revealed due to the simultaneously reduced V_{OC}, J_{SC} and FF, which could be attributed to the poor charge mobility of PEIE. For the P-ZnO-based OSCs, a highest PCE of 14.78% was achieved with a slightly increased J_{SC} of 22.96 mA cm^{-2} and a notably improved FF of 76.62%. To confirm the accuracy of *J-V* measurements, the corresponding EQE curves of OSCs were tested as shown in Fig. 4c. The calculated values of J_{SC} are summarized in Table 1, which are matched well with the measured ones. It is worth noting that the P-ZnO-based device substantially exhibits a distinct enhanced response in the region of 450–800 nm as compared with the reference device, which directly induces the improved photocurrent. To further understand the improvement of photoresponse in the range of 450–800 nm, optical simulations based on the transfer matrix formalism (TMF) method were performed. For a multilayered system, the energy distribution (Q) of each layer is a function of wavelength (λ) and position (x), which can be calculated by Equation (1):

$$Q(x,y) = 0.5\varepsilon_0 c\alpha|E(x)|^2, \quad (1)$$

where c is the speed of light, ε_0 is the permittivity of vacuum, α is the absorption coefficient, and $|E(x)|$ is the optical electric field [49]. The two-dimensional (2D) color filled contour plots of the calculated squared optical electric field strength $|E(x)|^2$ distribution for the ZnO- and P-ZnO-based devices are exhibited in Fig. 5a, b. Consequently, light intensity at 450–800 nm wavelength in the P-ZnO/BHJ layer is apparently higher than that of ZnO/BHJ layer, which is in according with the EQE result [52–55]. The exciton generation rate within PBDB-T/DTPPSe-2F film was calculated with different ETLs through optical simulations as shown in Figs S4, S5. Indeed, the exciton generation rate of P-ZnO/PBDB-T/DTPPSe-2F film also presents an enhancement than that of ZnO-based one. The enhanced photon harvesting in P-ZnO-based OSCs is ascribed to the porous structure which could soften reflection at the interface.

To analyze the accurate photon harvesting of OSCs, the absorption of active layer in the device was conducted to investigate the parasitic photon loss. The control devices were fabricated with poly(methyl methacrylate) (PMMA) instead of the PBDB-T/DTPPSe-2F blend for eliminating other effects [56]. The reflection spectra of all devices are shown in Fig. 5c. Clearly, the P-ZnO-based control device has a higher reflection than the ZnO-based counterpart. Whereas, the P-ZnO-based OSC presents a lower reflection in the cell. These results manifest that enhanced light trapping can occur in the P-ZnO-based OSCs due to the unique porous structure. The calculated absorption and light harvesting efficiency of active layer in devices are shown in Fig. 5d, and the detailed calculation methods are summarized in the Supplementary information. It is evident that more incident photons can be absorbed by the PBDB-T/DTPPSe-2F blend when employing the P-ZnO layer, which accounts for the increased J_{SC} in devices [57,58].

To analyze the variation of charge recombination properties in the derived devices, the dependences of J_{SC} and V_{OC} *versus* light intensity (P_{light}) were studied. As shown in Fig. S3f, the P_{light} dependence of J_{SC} is described as $J_{SC} \propto P_{light}^{\alpha}$, where the power-law exponent α reflects the bimolecular recombination behavior in device. The α values of ZnO- and P-ZnO-based devices are 0.96 and 0.99, respectively, indicating the bimolecular recombination is effectively suppressed in the P-ZnO-based OSCs. Through analyzing the relationship between V_{OC} and P_{light} in Fig. 5e, the slopes of V_{OC} *versus* $\ln(P_{light})$ for ZnO- and P-ZnO-based devices are $1.32kT/q$ and $1.12kT/q$, respectively, where k is the Boltzmann constant, T is Kelvin temperature, and q is the trap-assisted charge recombination which can be suppressed in the P-ZnO-based OSCs. The charge collection and exciton dissociation can be investigated from the dependence of photogenerated current density (J_{ph}) on effective voltage (V_{eff}).

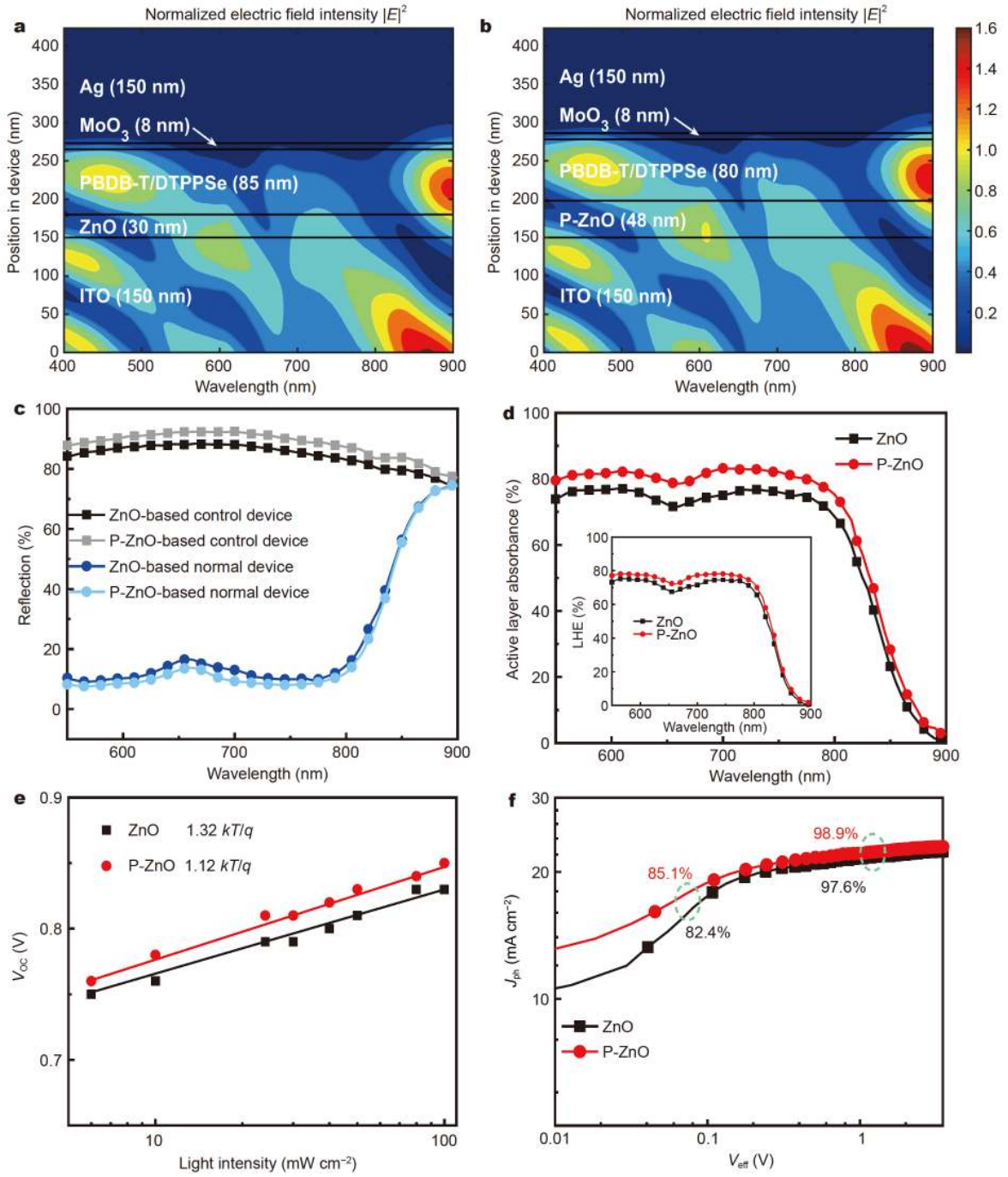

Figure 5 2D color filled contour plots of the normalized optical electric field $|E(x)|^2$ for (a) ZnO- and (b) P-ZnO-based devices, respectively. (c) Reflection spectra of normal and control devices. (d) Absorption spectra of active layers in cells. The reduced figure illustrates the light harvesting efficiency. (e) V_{OC} *versus* light intensity and (f) J_{ph}-V_{eff} characteristics for ZnO- and P-ZnO-based OSCs using PBDB-T/DTPPSe-2F as active layer.

The exciton dissociation and charge collection efficiency can be evaluated by the values of J_{ph}/J_{sat} under short-circuit current and maximal output conditions, where J_{sat} is the saturation photocurrent [59–61]. Herein, the pseudo J_{sat} values were selected at 2.1 V reverse bias for equitable comparison. As shown in Fig. 5f, the J_{ph}/J_{sat} values under short-circuit current and maximal output conditions were calculated to be 97.6% and 82.4% for

ZnO-based device, 98.9% and 85.1% for P-ZnO-based device, respectively. The higher J_{ph}/J_{sat} values of P-ZnO-based devices indicate more efficient exciton dissociation and charge collection, which can arouse the improved J_{SC} and FF.

Long-term storage stability and generality of P-ZnO-based OSCs

The long-term storage stability of PBDB-T/DTPPSe-2F-based OSCs was also performed. The P-ZnO-based devices without encapsulation present enhanced storage stability whether in the N_2 or ambient air condition, as shown in Fig. 6a, b and Figs S6, S7. The P-ZnO/PBDB-T/DTPPSe-2F-based device can maintain its initial efficiency of 90% after 1000 h of storage in N_2, while only 72% of its original PCE can be obtained for ZnO-based device. In the air condition, the P-ZnO-based device also reveals laudable storage stability, delivering a PCE of 12.41% (86% of its original performance) after 1000 h aging. Inspired by the superior storage stability in ambient air, all air-processed OSCs were fabricated. The photovoltaic parameters are provided in Table S4, and the related *J*-*V* and EQE curves are plotted in Fig. 6c, d. For the air-processed OSCs, the P-ZnO-based device also achieved an enhanced photoresponse and a higher PCE of 14.13% than that of ZnO-based one (12.35%). The promising PCE of 14.13% is among the highest efficiencies reported for air-processed OSCs in the literature as summarized in Tables S5, S6.

To explore the generality of P-ZnO serving as ETL for efficient OSCs, two frequently used BHJ systems (PM6/Y6 and PTB7-Th/$PC_{71}BM$) were utilized as shown in Fig. 7a. For an intuitional comparison, OSCs using ZnO as ETL were also carried out. As summarized in Fig. 7 and Table 1, the P-ZnO-based devices indeed present higher efficiencies compared with the counterparts. In the contrast, for the ZnO-based device, the PCEs of 15.38% and 9.12% were achieved for PM6/Y6- and PTB7-Th/$PC_{71}BM$-based OSCs, respectively, which are close to the reported value in the literatures [46,47]. Herein, the P-ZnO/PM6/Y6-based device achieved an optimal PCE of 16.57% with simultaneously increased J_{SC} of 25.70 mA cm^{-2} and FF of 75.84%. An enhancement of 8% in PCE (from 9.12% to 9.85%) can also be achieved in the representative PTB7-Th/$PC_{71}BM$-based OSCs with similar improvement. These results demonstrate the gen-

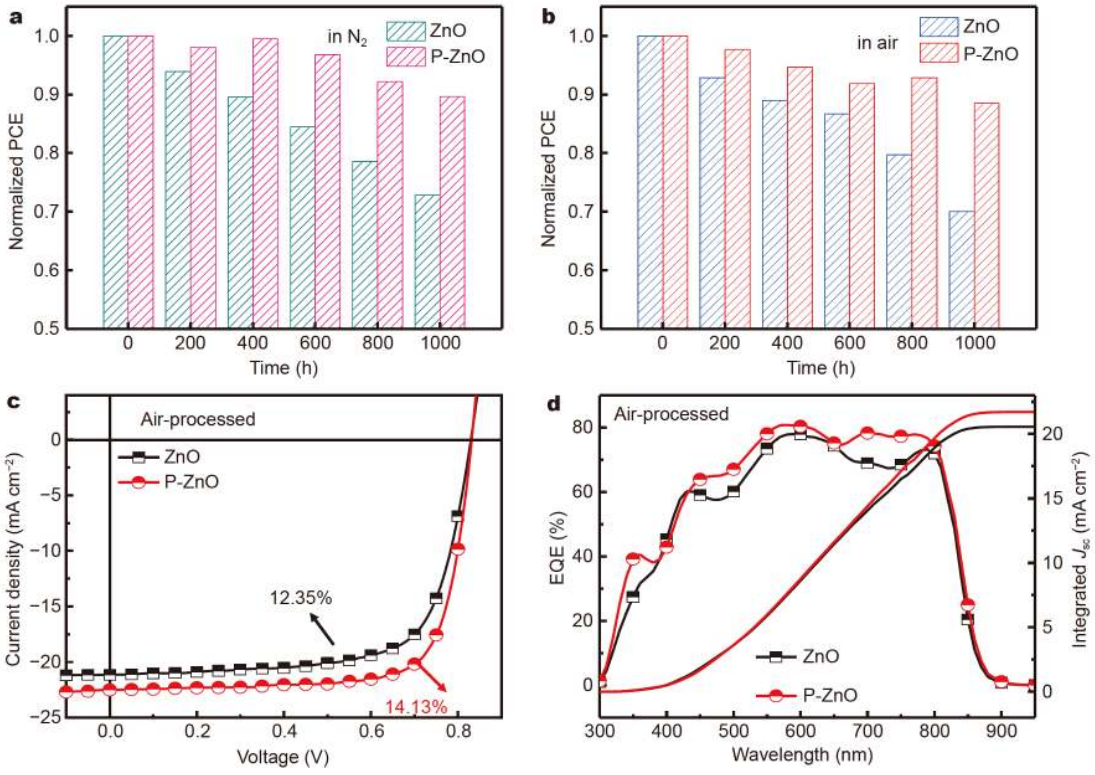

Figure 6 The variation of PCEs for ZnO- and P-ZnO-based OSCs using PBDB-T/DTPPSe-2F as active layer after aging in (a) N_2 and (b) air. (c) *J*-*V* curves and (d) EQE curves of the air-processed OSCs using PBDB-T/DTPPSe-2F as active layer with different ETLs.

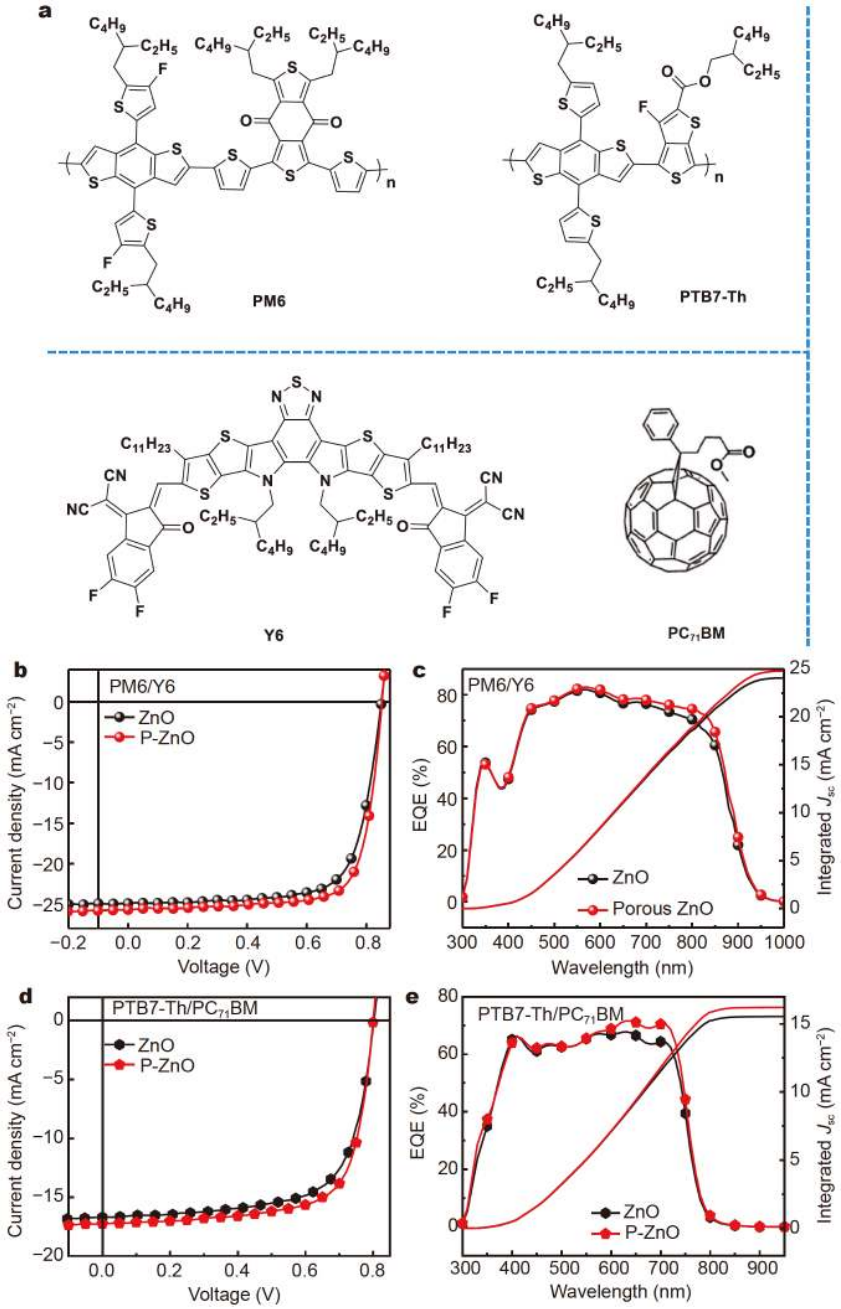

Figure 7 (a) The chemical structures of PM6, Y6, PTB7-Th and $PC_{71}BM$. (b) *J-V* curves and (c) EQE curves of PM6/Y6-based OSCs with different ETLs. (d) *J-V* curves and (e) EQE curves of PTB7-Th/$PC_{71}BM$-based OSCs with different ETLs, respectively.

erality of P-ZnO serving as ETL for efficient OSCs.

CONCLUSION

In summary, a porous inorganic/organic (ZnO/PEIE) hybrid ETL, P-ZnO can be successfully adopted for efficient OSCs. The derived P-ZnO presents a unique porous surface feature with distinct distribution with residual PEIE mainly at the bottom of ETL. And a reduced work function of P-ZnO is induced, which is beneficial to the suppressed charge recombination and enhanced charge extraction in devices. P-ZnO-based OSCs also present an enhanced light trapping in the active layer compared with ZnO-based counterparts. The increased light harvesting efficiency can account for the increased J_{SC}. Conse-

quently, the enhancements of 8% in PCEs have been achieved with enhanced J_{SC} and FF for P-ZnO-based OSCs, delivering higher PCEs of 14.78%, 9.85% and 16.57% for devices based on PBDB-T/DTPPSe-2F, PTB7-Th/$PC_{71}BM$ and PM6/Y6, respectively. The P-ZnO/PBDB-T/DTPPSe-2F-based OSCs without encapsulation also present improved long-term storage stability whether in the N_2 or ambient air condition. Furthermore, the air-processed OSCs based on P-ZnO/PBDB-T/DTPPSe-2F possess a promising PCE of 14.13%, which is among the highest efficiencies reported for air-processed OSCs in the literature. These results demonstrate the great potential of the porous hybrid P-ZnO as ETL for constructing high-performance and air-stable OSCs.

Received 20 July 2020; accepted 26 August 2020; published online 15 December 2020

1 Song Y, Zhang K, Dong S, *et al.* Semitransparent organic solar cells enabled by a sequentially deposited bilayer structure. ACS Appl Mater Interfaces, 2020, 12: 18473–18481
2 Qin J, An C, Zhang J, *et al.* 15.3% Efficiency all-small-molecule organic solar cells enabled by symmetric phenyl substitution. Sci China Mater, 2020, 63: 1142–1150
3 Wang H, Cao J, Yu J, *et al.* Molecular engineering of central fused-ring cores of non-fullerene acceptors for high-efficiency organic solar cells. J Mater Chem A, 2019, 7: 4313–4333
4 Yan C, Barlow S, Wang Z, *et al.* Non-fullerene acceptors for organic solar cells. Nat Rev Mater, 2018, 3: 18003
5 Hou J, Inganäs O, Friend RH, *et al.* Organic solar cells based on non-fullerene acceptors. Nat Mater, 2018, 17: 119–128
6 Liu Q, Jiang Y, Jin K, *et al.* 18% Efficiency organic solar cells. Sci Bull, 2020, 65: 272–275
7 An Q, Wang J, Gao W, *et al.* Alloy-like ternary polymer solar cells with over 17.2% efficiency. Sci Bull, 2020, 65: 538–545
8 Zhan L, Li S, Lau TK, *et al.* Over 17% efficiency ternary organic solar cells enabled by two non-fullerene acceptors working in an alloy-like model. Energy Environ Sci, 2020, 13: 635–645
9 Cui Y, Yao H, Zhang J, *et al.* Single-junction organic photovoltaic cells with approaching 18% efficiency. Adv Mater, 2020, 32: 1908205
10 Yue Q, Wu H, Zhou Z, *et al.* 13.7% Efficiency small-molecule solar cells enabled by a combination of material and morphology optimization. Adv Mater, 2019, 31: 1904283
11 Jia T, Zhang J, Zhong W, *et al.* 14.4% Efficiency all-polymer solar cell with broad absorption and low energy loss enabled by a novel polymer acceptor. Nano Energy, 2020, 72: 104718
12 Qiu B, Chen Z, Qin S, *et al.* Highly efficient all-small-molecule organic solar cells with appropriate active layer morphology by side chain engineering of donor molecules and thermal annealing. Adv Mater, 2020, 32: 1908373
13 Wan J, Zhang L, He Q, *et al.* High-performance pseudoplanar heterojunction ternary organic solar cells with nonfullerene alloyed acceptor. Adv Funct Mater, 2020, 30: 1909760
14 Sun H, Liu T, Yu J, *et al.* A monothiophene unit incorporating both fluoro and ester substitution enabling high-performance donor polymers for non-fullerene solar cells with 16.4% efficiency. Energy Environ Sci, 2019, 12: 3328–3337
15 Wang H, Zhang Z, Yu J, *et al.* Nonacyclic carbazole-based non-fullerene acceptors enable over 12% efficiency with enhanced stability for organic solar cells. J Mater Chem A, 2019, 7: 21903–21910
16 Wang Y, Wang Y, Zhu L, *et al.* A novel wide-bandgap small molecule donor for high efficiency all-small-molecule organic solar cells with small non-radiative energy losses. Energy Environ Sci, 2020, 13: 1309–1317
17 Cui Y, Yao H, Zhang J, *et al.* Over 16% efficiency organic photovoltaic cells enabled by a chlorinated acceptor with increased open-circuit voltages. Nat Commun, 2019, 10: 2515
18 Xu C, Wang J, An Q, *et al.* Ternary small molecules organic photovoltaics exhibiting 12.84% efficiency. Nano Energy, 2019, 66: 104119
19 Wang H, Zhang Z, Yu J, *et al.* Over 15% efficiency in ternary organic solar cells by enhanced charge transport and reduced energy loss. ACS Appl Mater Interfaces, 2020, 12: 21633–21640
20 Zhu L, Zhong W, Qiu C, *et al.* Aggregation-induced multilength scaled morphology enabling 11.76% efficiency in all-polymer solar cells using printing fabrication. Adv Mater, 2019, 31: 1902899
21 Zhu L, Zhang M, Zhou G, *et al.* Efficient organic solar cell with 16.88% efficiency enabled by refined acceptor crystallization and morphology with improved charge transfer and transport properties. Adv Energy Mater, 2020, 10: 1904234
22 Ma X, Wang J, An Q, *et al.* Highly efficient quaternary organic photovoltaics by optimizing photogenerated exciton distribution and active layer morphology. Nano Energy, 2020, 70: 104496
23 Gao K, Jo SB, Shi X, *et al.* Over 12% efficiency nonfullerene all-small-molecule organic solar cells with sequentially evolved multilength scale morphologies. Adv Mater, 2019, 31: 1807842
24 Wang C, Moro F, Ni S, *et al.* Thermal-annealing effects on energy level alignment at organic heterojunctions and corresponding voltage losses in all-polymer solar cells. Nano Energy, 2020, 72: 104677
25 Liang X, Bai S, Wang X, *et al.* Colloidal metal oxide nanocrystals as charge transporting layers for solution-processed light-emitting diodes and solar cells. Chem Soc Rev, 2017, 46: 1730–1759
26 Li X, Zhang W, Usman K, *et al.* Small molecule interlayers in organic solar cells. Adv Energy Mater, 2018, 8: 1702730
27 Huang Z, Ouyang D, Shih CJ, *et al.* Solution-processed ternary oxides as carrier transport/injection layers in optoelectronics. Adv Energy Mater, 2020, 10: 1900903
28 Oh H, Krantz J, Litzov I, *et al.* Comparison of various sol-gel derived metal oxide layers for inverted organic solar cells. Sol Energy Mater Sol Cells, 2011, 95: 2194–2199
29 Richardson BJ, Wang X, Almutairi A, *et al.* High efficiency PTB7-based inverted organic photovoltaics on nano-ridged and planar zinc oxide electron transport layers. J Mater Chem A, 2015, 3: 5563–5571
30 Ma H, Yip HL, Huang F, *et al.* Interface engineering for organic electronics. Adv Funct Mater, 2010, 20: 1371–1388
31 Zhang D, Choy WCH, Xie F, *et al.* Plasmonic electrically functionalized TiO_2 for high-performance organic solar cells. Adv Funct Mater, 2013, 23: 4255–4261
32 MacLeod BA, Tremolet de Villers BJ, Schulz P, *et al.* Stability of inverted organic solar cells with ZnO contact layers deposited from precursor solutions. Energy Environ Sci, 2015, 8: 592–601
33 Sun Y, Seo JH, Takacs CJ, *et al.* Inverted polymer solar cells integrated with a low-temperature-annealed sol-gel-derived ZnO film as an electron transport layer. Adv Mater, 2011, 23: 1679–1683

34 Jin WY, Ginting RT, Jin SH, *et al.* Highly stable and efficient inverted organic solar cells based on low-temperature solution-processed PEIE and ZnO bilayers. J Mater Chem A, 2016, 4: 3784–3791
35 Li Z, Chueh CC, Jen AKY. Recent advances in molecular design of functional conjugated polymers for high-performance polymer solar cells. Prog Polym Sci, 2019, 99: 101175
36 Lin PC, Wong YT, Su YA, *et al.* Interlayer modification using eco-friendly glucose-based natural polymers in polymer solar cells. ACS Sustain Chem Eng, 2018, 6: 14621–14630
37 Pan F, Sun C, Li Y, *et al.* Solution-processable N-doped graphene-containing cathode interfacial materials for high-performance organic solar cells. Energy Environ Sci, 2019, 12: 3400–3411
38 Zhang K, Xia R, Fan B, *et al.* 11.2% all-polymer tandem solar cells with simultaneously improved efficiency and stability. Adv Mater, 2018, 30: 1803166
39 Lee BH, Jung IH, Woo HY, *et al.* Multi-charged conjugated polyelectrolytes as a versatile work function modifier for organic electronic devices. Adv Funct Mater, 2014, 24: 1100–1108
40 He Z, Xiao B, Liu F, *et al.* Single-junction polymer solar cells with high efficiency and photovoltage. Nat Photon, 2015, 9: 174–179
41 Zhou Y, Fuentes-Hernandez C, Shim J, *et al.* A universal method to produce low-work function electrodes for organic electronics. Science, 2012, 336: 327–332
42 Goo JS, Shin SC, You YJ, *et al.* Polymer surface modification to optimize inverted organic photovoltaic devices under indoor light conditions. Sol Energy Mater Sol Cells, 2018, 184: 31–37
43 Li P, Wang G, Cai L, *et al.* High-efficiency inverted polymer solar cells controlled by the thickness of polyethylenimine ethoxylated (PEIE) interfacial layers. Phys Chem Chem Phys, 2014, 16: 23792–23799
44 Cao J, Qu S, Yu J, *et al.* 13.76% efficiency nonfullerene solar cells enabled by selenophene integrated dithieno[3,2-*b*:2′,3′-*d*]pyrrole asymmetric acceptors. Mater Chem Front, 2020, 4: 924–932
45 Yuan J, Zhang Y, Zhou L, *et al.* Single-junction organic solar cell with over 15% efficiency using fused-ring acceptor with electron-deficient core. Joule, 2019, 3: 1140–1151
46 Park S, Cha MJ, Seo JH, *et al.* Treating the poly(3,4-ethylenedioxythiophene):poly(styrenesulfonate) surface with hydroquinone enhances the performance of polymer solar cells. ACS Appl Mater Interfaces, 2018, 10: 41578–41585
47 Yan Y, Li W, Cai J, *et al.* Improved efficiency in fullerene and non-fullerene polymer solar cells having an interdigitated interface with the electron transport layer. Mater Chem Front, 2018, 2: 1859–1865
48 Wang C, Li C, MacKenzie RCI, *et al.* Polyelectrolyte interlayers with a broad processing window for high efficiency inverted organic solar cells towards mass production. J Mater Chem A, 2018, 6: 17662–17670
49 Zhang Z, Zhang Z, Zhao B, *et al.* Polymer with a 3D conductive network: A thickness-insensitive electron transport layer for inverted polymer solar cells. J Mater Chem A, 2018, 6: 12969–12973
50 Sun R, Deng D, Guo J, *et al.* Spontaneous open-circuit voltage gain of fully fabricated organic solar cells caused by elimination of interfacial energy disorder. Energy Environ Sci, 2019, 12: 2518–2528
51 Woo S, Hyun Kim W, Kim H, *et al.* 8.9% Single-stack inverted polymer solar cells with electron-rich polymer nanolayer-modified inorganic electron-collecting buffer layers. Adv Energy Mater, 2014, 4: 1301692
52 Zou J, Yip HL, Zhang Y, *et al.* High-performance inverted polymer solar cells: Device characterization, optical modeling, and hole-transporting modifications. Adv Funct Mater, 2012, 22: 2804–2811
53 Wang F, Wang Y, Liu H, *et al.* Fine tuning the light distribution within the photoactive layer by both solution-processed anode and cathode interlayers for high performance polymer solar cells. Sol RRL, 2018, 2: 1800141
54 Chen KS, Salinas JF, Yip HL, *et al.* Semi-transparent polymer solar cells with 6% PCE, 25% average visible transmittance and a color rendering index close to 100 for power generating window applications. Energy Environ Sci, 2012, 5: 9551
55 Chueh CC, Chien SC, Yip HL, *et al.* Toward high-performance semi-transparent polymer solar cells: Optimization of ultra-thin light absorbing layer and transparent cathode architecture. Adv Energy Mater, 2013, 3: 417–423
56 Hu Z, Yang L, Gao W, *et al.* Over 15.7% efficiency of ternary organic solar cells by employing two compatible acceptors with similar LUMO levels. Small, 2020, 16: 2000441
57 Huyen Nguyen TM, Bark CW. Highly porous nanostructured NiO@C as interface-effective layer in planar n-i-p perovskite solar cells. J Alloys Compd, 2020, 841: 155711
58 Agrios AG, Hagfeldt A. Low-temperature TiO_2 films for dye-sensitized solar cells: Factors affecting energy conversion efficiency. J Phys Chem C, 2008, 112: 10021–10026
59 Wang J, Zheng Z, Zhang D, *et al.* Regulating bulk-heterojunction molecular orientations through surface free energy control of hole-transporting layers for high-performance organic solar cells. Adv Mater, 2019, 31: 1806921
60 Yang B, Zhang S, Li S, *et al.* A self-organized poly(vinylpyrrolidone)-based cathode interlayer in inverted fullerene-free organic solar cells. Adv Mater, 2019, 31: 1804657
61 Zheng Z, Hu Q, Zhang S, *et al.* A highly efficient non-fullerene organic solar cell with a fill factor over 0.80 enabled by a fine-tuned hole-transporting layer. Adv Mater, 2018, 30: 1801801

Acknowledgements This work was supported by the National Natural Science Foundation of China (21905137) and the Natural Science Foundation of Jiangsu Province (BK20180496).

Author contributions Yu J and Qu S conceived and designed the experiments; Cao J provided the acceptor DTPPSe-2F; Wang H and Guang S performed the morphology characterizations; Liu X performed the optical simulations; Yu J and Tang W directed the project. All authors contributed to the general discussion.

Conflict of interest The authors declare that they have no conflict of interest.

Supplementary information Supporting data are available in the online version of the paper.

Shenya Qu received her BSc degree from Nanjing Forest University. She has been pursuing her postgraduate degree in Nanjing University of Science and Technology since 2018. Her research interests focus on the device fabrication and optical optimization for interlayer modification in organic solar cells.

Jiangsheng Yu received his PhD degree in 2017 from Nanjing University of Science and Technology and the University of Washington. Then, he joined MIIT Key Laboratory of Advanced Solid Laser in Nanjing University of Science and Technology. His research mainly focuses on photovoltaic material development and device engineering on organic solar cells.

Weihua Tang has been a professor in Nanjing University of Science and Technology since 2009. He received his PhD degree in chemistry from National University of Singapore. His research interests mainly focus on molecular design of conjugated materials and device optimization for organic/perovskite solar cells and energy storage systems.

一种可增强光陷阱效应的多孔ZnO/PEIE电子传输层在高效有机太阳能电池中的应用

屈沈雅[1,2], 俞江升[1*], 曹金如[2], 刘鑫[1], 王宏涛[1,2], 光顺[1,2], 唐卫华[2*]

摘要 在本工作中，我们制备了一种多孔的有机/无机复合电子传输层(P-ZnO)，并将其成功用于反向有机太阳能电池中. P-ZnO不仅拥有适宜的功函，且可形成较大欧姆接触面积的独特表面，有利于器件中的电荷提取. 与ZnO基器件相比，P-ZnO基器件的活性层具有增强的光陷阱效应. 在PBDB-T/DTPPSe-2F，PM6/Y6和PTB7-Th/$PC_{71}BM$三个活性层体系中，基于P-ZnO的器件都可实现8%增幅的效率提升. 尤其是P-ZnO/PBDB-T/DTPPSe-2F的未封装器件无论在氮气还是空气氛围下，均表现出良好的长期稳定性. 在空气中制备的P-ZnO/PBDB-T/DTPPSe-2F器件仍可实现14.13%的高效率，这是目前文献报道的空气氛围制备有机太阳能电池的最高效率之一. 实验结果表明，P-ZnO作为电子传输层在构建高性能和空气稳定的有机太阳能电池方面具有巨大的应用潜力.

